Journal of Materials Science: Materials in Electronics (2020) 31:6140–6149
https://doi.org/10.1007/s10854-020-03167-3

Synthesis of Ni_3Se_2 on nickel foam with different morphologies for high-performance supercapacitor electrode

Liting Wu[1] · Yonggang Xue[1] · Han Chen[1] · Kaiyou Zhang[1] · Aimiao Qin[1] · Shuoping Chen[1]

Received: 14 May 2019 / Accepted: 24 February 2020 / Published online: 4 March 2020

Abstract

The Ni_3Se_2 grown on nickel foam (Ni_3Se_2@Ni) with irregular film, nanowire arrays and microsphere morphologies were successfully synthesized using different reagents via simple one-step hydrothermal method. The as-prepared Ni_3Se_2@Ni can be used as the electrode for supercapacitor directly without further processing, and the results showed that the Ni_3Se_2 with the morphologies of irregular film, nanowire arrays and microsphere exhibited the specific capacitance of 1.26 F/cm^2 (504 F/g), 1.48 F/cm^2 (592 F/g) and 2.04 F/cm^2 (816 F/g) at the current density of 10 mA/cm^2 in 3 M KOH electrolyte, respectively. Comparing the electrochemical performance of Ni_3Se_2@Ni electrode with different morphologies, the Ni_3Se_2 microsphere displayed better electrochemical performance, which exhibited the long-term stability with 85.5% of specific capacitance retention after 1000 cycles. The results indicated that the as-prepared Ni_3Se_2@Ni can be used as a promising electrode for energy storage devices.

1 Introduction

In recent years, supercapacitors have attracted more and more attention due to its high power density, fast charge/discharge rate and long cycle life [1–3]. Therefore, a large number of materials have been explored for supercapacitor electrodes. Generally speaking, the electrode materials of supercapacitors mainly contain carbon-based materials [4–7], transition metal oxide materials [8] and conductive polymer materials [9, 10]. The carbon-based materials (such as activated carbon, carbon nanotubes, graphene, and so on) exhibit larger specific surface area and longer cycle life. Nevertheless, the lower energy density has limited its development. In contrast, the conductive polymer materials usually present higher specific capacitance than carbon-based materials [11]. However, in the process of charging/discharging, a certain degree of volume expansion or contraction will occur and result in poor stability [12]. Compared with carbon-based materials and conductive polymer materials, the transition metal oxides can not only store charges by electrostatic adsorption but also store more charges by Faraday reaction, thus obtaining higher energy density [13]. Therefore, transition metal oxide materials are undoubtedly a better choice for the supercapacitor electrode. For example, He et al. [14] synthesized the CuO with the three-dimensional flower-like morphology on a copper foam, which achieved a high-specific capacitance of 1641.4 mF/cm^2 at the current density of 2 mA/cm^2 and good cycling stability with 79% retention after 10,000 charge/discharge cycles. Furthermore, Sun et al. [15] prepared the NiO nanocubes by simple hydrothermal route and assembled the NiO//AC (activated carbon) asymmetric supercapacitor, which exhibited the specific capacitance of 1012 mF/cm^2 at the current density of 1 mA/cm^2 and good cycle performance with 89.3% of specific capacitance retention after 10,000 charge/discharge cycles.

However, in the process of electrochemistry, the selenium (Se) shows better metallic property than oxygen (O), which indicates the better electronic property of Se [16, 17]. Thus, nickel selenide as one of the transition metal selenides has been widely applied to dye-sensitized solar cells [18],

Electronic supplementary material The online version of this article (https://doi.org/10.1007/s10854-020-03167-3) contains supplementary material, which is available to authorized users.

✉ Kaiyou Zhang
kaiyou2014@glut.edu.cn

[1] Guangxi Ministry-Province Jointly-Constructed Cultivation Base for State Key Laboratory of Processing for Non-Ferrous Metal and Featured Materials, Guangxi Key Laboratory of Optical and Electronic Materials and Devices, College of Materials Science and Engineering, Guilin University of Technology, Guilin 541004, People's Republic of China

electrocatalyst [19], lithium-ion/sodium-ion battery [20], and supercapacitor [21, 22] due to its excellent physical and chemical properties. As electrode materials for supercapacitors, the $NiSe_2$ prepared by Wang et al. [23] exhibited a high-specific capacitance of 1044 F/g at a current density of 3 A/g. And the $Ni_{0.85}Se$ grown on Ni foam showed the specific capacitance of 1115 F/g at a current density of 1 A/g [21], which can be used as a high-performance electrode for supercapacitors. In addition, other transition metal selenides have also been studied as supercapacitor materials. Tian et al. [24] fabricated the NiSe nanorod arrays by the hydrothermal method and demonstrated its excellent electrochemical performance with areal specific capacitance of 6.81 F/cm^2 at a current density of 5 mA/cm^2. The high specific capacitance of NiSe can be attributed to the metallic conductivity of nickel selenides, the short ions diffusion length from the electrolyte to electrode materials, and fast electronic transmission path between active materials and collectors. In addition, the Ni_3Se_2 grown on nickel foam was synthesized for the first time by Jiang et al. [25] via hydrothermal method, exhibiting an excellent specific capacitance of 854 F/g at a current density of 1 A/g. These reports indicated that the nickel selenide would have a promising application prospect as the electrode materials of supercapacitors. Moreover, to improve the electrochemical performance, the morphology of the materials, as one of the significant influencing factors, has also been the research focus in recent years [26]. For example, Ma et al. [27] obtained the flower-like, nanoparticle and ball-like $Ni_{0.85}Se$ by changing the amount of ethylenediamine (EDA) and explored their electrochemical performances. The results showed that the electrochemical performances of flower-like structure $Ni_{0.85}Se$ were better than that of the nanoparticles and ball-like morphology, as the flower-like structure possessing more available sites. Thus, controlling and changing the morphology of Ni_3Se_2 may improve its electrochemical performance and it can be used as a prospective material for supercapacitors.

In this study, the Ni_3Se_2 grown on the nickel foam (Ni_3Se_2@Ni) with different morphologies were designed by a simple one-step hydrothermal method with adding different reagents. The Ni_3Se_2@Ni with the morphologies of irregular film, nanowire arrays and microsphere were obtained, and the corresponding areal specific capacitance was 1.26 F/cm^2, 1.48 F/cm^2 and 2.04 F/cm^2 at the current density of 10 mA/cm^2 in 3 M KOH electrolyte, respectively. The results indicated that the Ni_3Se_2 microsphere had better electrochemical performance, and the specific capacitance still retained 85.54% after 1000 cycles.

2 Experimental

2.1 Synthesis of Ni_3Se_2

The Ni_3Se_2 with different morphologies were synthesized by hydrothermal method. The chemical reagents used were analytical grade and were used without further purification. The nickel foam slices ($1.5 \times 3.0 \times 0.1$ cm^3) were washed with toluene, acetone, ethanol, 2.4 M HCl and deionized water successively, and then dried in a vacuum oven at 60 °C for 2 h. Typically, 0.1 mmol of Se powder and 2 mL of $N_2H_4 \cdot H_2O$ (80 wt%) were dissolved in 13 mL of deionized water in a 25 mL Teflon vessel, then a slice of nickel foam was put into the above Teflon vessel and sealed in a stainless-steel autoclave. Later, it was put in the furnace with temperature of 160 °C for 12 h. After it was cooled down to room temperature naturally, the product was taken out and rinsed with deionized water and ethanol several times and dried in a vacuum oven at 60 °C for 2 h, and finally the irregular film of Ni_3Se_2 was obtained, which was named as Ni_3Se_2-A. In addition, nanowire arrays and microsphere of Ni_3Se_2 were prepared in a similar route by varying the reaction reagents and temperature. The nanowire arrays of Ni_3Se_2 (named as Ni_3Se_2-B) can be obtained by increasing the dosage of Se powder to 0.4 mmol and adding 0.2 mmol of $Ni(NO_3)_2$ with temperature of 140 °C. Similarly, the Ni_3Se_2 microsphere (named as Ni_3Se_2-C) were synthesized by dissolving 0.2 mmol of Se powder, 2 mL of $N_2H_4 \cdot H_2O$ and 2 mL of EDA in 11 mL of deionized water with the reaction temperature of 140 °C. The loading masses of Ni_3Se_2 with different morphologies were measured to be about 2.5 mg/cm^2. For comparison, the samples with different temperatures of 140 °C, 160 °C and 180 °C were also investigated (Supplementary material).

2.2 Characterization of the samples

The samples were characterized by X-ray diffraction (XRD, PANalytical X'Pert) with Cu Kα radiation (λ= 1.5406 Å) and field-emission scanning electron microscope (FE-SEM, S-4800) with an energy disperse spectroscopy (EDS, X-max50) attachment. The Brunauer–Emmett–Teller (BET) specific surface areas and the pore size distribution according to the Barrett–Joyner–Halenda (BJH) methods of the samples were performed by the Micromeritics ASAP 2020 HD88 apparatus. And the electrochemical performance was characterized by electrochemical workstation (CHI690) in 3 M KOH electrolyte using three-electrode configuration, where the effective electrode contact area was 1×1 cm^2, a platinum foil with area of 1×1 cm^2

and an Hg/HgO electrode were used as the counter and reference electrodes, respectively.

3 Results and discussion

The as-prepared Ni_3Se_2 on nickel foam with different morphologies were first characterized by XRD and the corresponding XRD patterns were shown in Fig. 1a. Comparing the three diffraction patterns, we can see that the diffraction patterns of Ni_3Se_2-A (irregular film), Ni_3Se_2-B (nanowire arrays) and Ni_3Se_2-C (microsphere) are almost the same. The three strongest diffraction peaks located at 2θ of 44.51°, 51.85° and 76.37° can be assigned to the substrate of nickel foam (JCPDS no. 04-0850) with the corresponding crystal indices of (110), (200) and (220). Except for the peaks of nickel foam, the other diffraction peaks at 2θ of 20.94°, 29.59°, 29.97°, 37.17°, 42.62°, 47.68°, 48.20°, 52.74° and 53.46° were consistent with the rhombohedral phase of Ni_3Se_2 (JCPDS no. 85-0754) with lattice constant of $a = b = 6.03382$ Å and $c = 7.25102$ Å, and the corresponding crystal indices were (101), (110), (012), (003), (202), (211), (113), (122) and (104), respectively. In addition, the EDS of Ni_3Se_2-A, Ni_3Se_2-B and Ni_3Se_2-C were displayed in Fig. 1b–d, respectively. The results showed that all the samples mainly consisted of Se and Ni elements, however, there was also a little O element appearing in the spectra, which was possibly due to the moisture and oxygen adsorbed on the surface of samples [21].

The different morphologies of Ni_3Se_2 grown on nickel foam were investigated by FE-SEM. Figure 2a–c show the low-magnification FE-SEM images of Ni_3Se_2-A, Ni_3Se_2-B and Ni_3Se_2-C, respectively, and Fig. 2d–f present the corresponding high-magnification FE-SEM images. It can be seen from the low-magnification image of Fig. 2a that the morphology of Ni_3Se_2-A is a rough film, and the high-magnification image of Fig. 2d shows that the surface of the film is irregular, which looks like angular gravel. Figure 2b, e shows the FE-SEM images of Ni_3Se_2-B, it is observed that the Ni_3Se_2 nanowires are grown in-situ on nickel foam surface with the length of ca. 1 μm and diameter of ca. 100 nm, presenting the nanowire arrays morphology. In addition, Fig. 2c shows the low-magnification FE-SEM image of Ni_3Se_2-C, which exhibits the uniform microsphere morphology with a diameter of ca. 2 μm. However, the microspheres display rough surface in Fig. 2f, which can be inferred that the microsphere might consist of smaller particles. The schematic diagram of the synthesis of Ni_3Se_2 with different morphology is demonstrated in Fig. 2g. As described in the experimental section, when $N_2H_4{\cdot}H_2O$ was put in the mixture containing Se, the Se can be rapidly reduced during heating, causing explosive growth of Ni_3Se_2 to form the irregular film on the surface of nickel foam [27]. And when the Ni^{2+} was added in the hydrazine hydrate solution, the Ni^{2+} would react with the Se^{2+} in solution to construct Ni_3Se_2 crystal nucleus and grow perpendicular to the nickel foam surface to form the nanowire arrays [24]. However, with the addition of EDA, the interaction between the different crystal faces was enhanced and the thermodynamic stability of the spherical structure will occur [27]. Afterwards, the Ni_3Se_2 spheres grow isochronously, resulting in the formation of microsphere morphology.

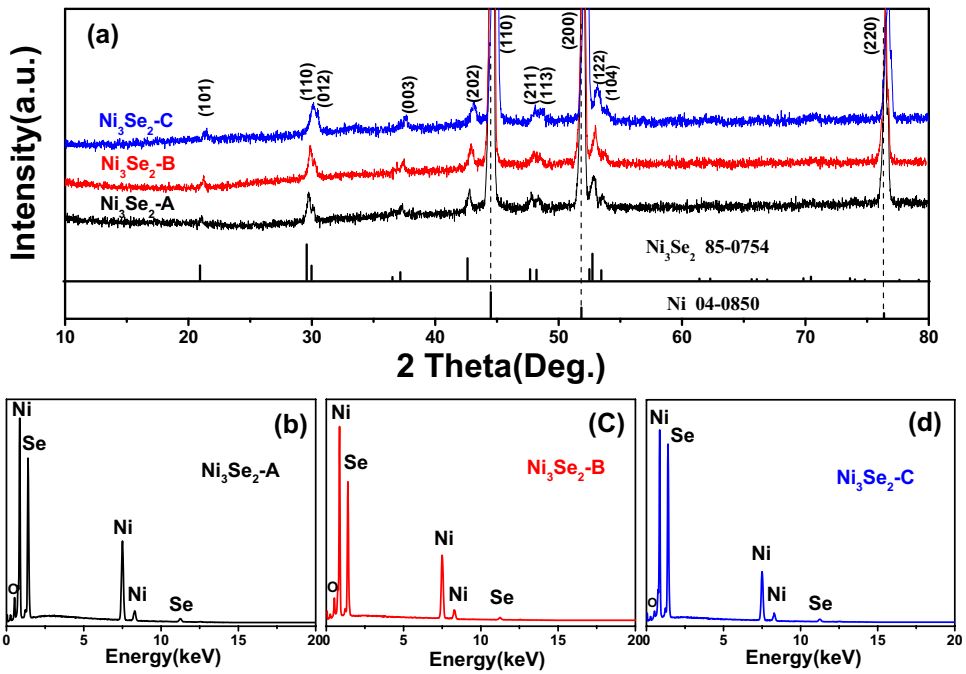

Fig. 1 XRD patterns and EDS of Ni_3Se_2 with different morphologies: **a** XRD patterns, **b–d** EDS: **b** Ni_3Se_2-A, **c** Ni_3Se_2-B, **d** Ni_3Se_2-C

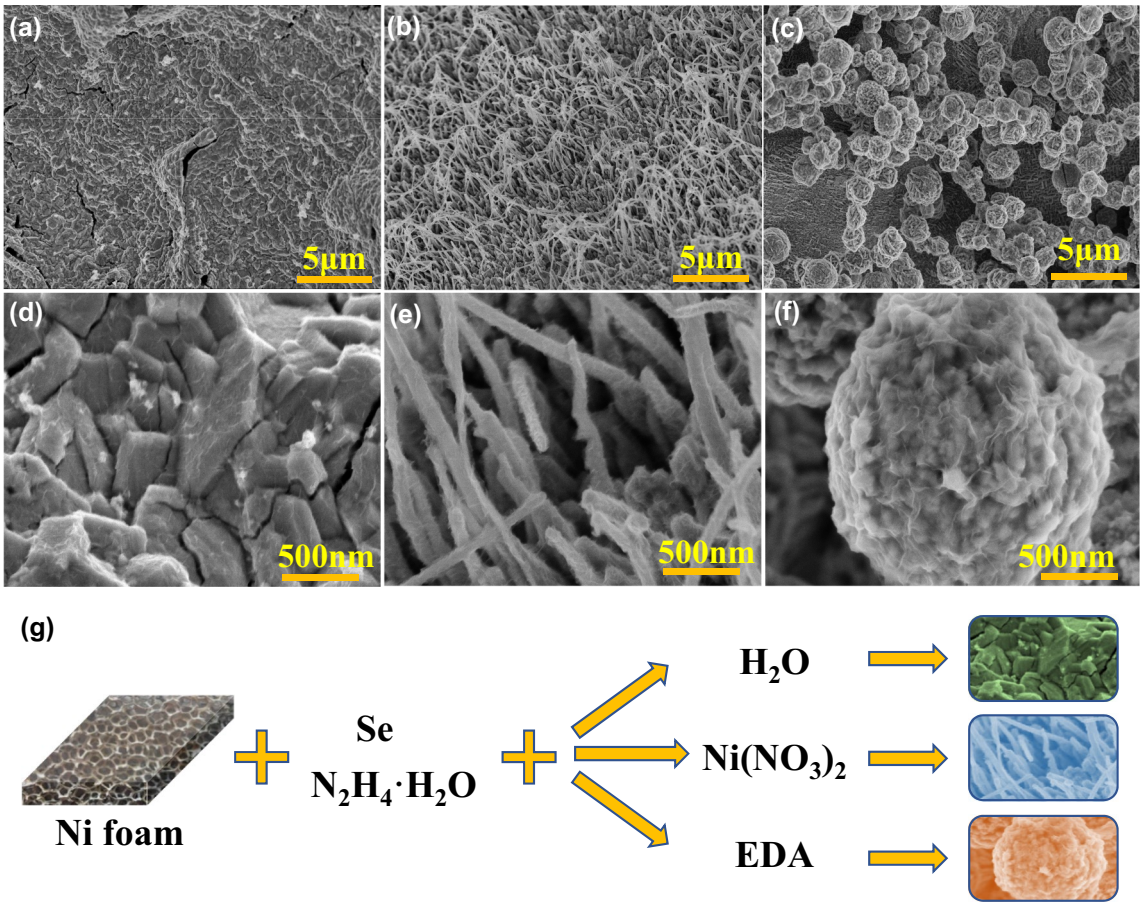

Fig. 2 FE-SEM images of Ni_3Se_2 with different morphologies: **a**, **d** Ni_3Se_2-A irregular film, **b**, **e** Ni_3Se_2-B nanowire arrays, **c**, **f** Ni_3Se_2-C microsphere; **g** schematic illustration of the synthesis of Ni_3Se_2 with different morphologies

The Ni_3Se_2 can be obtained in a certain temperature range from 140 to 180 °C in this work. And the XRD patterns and FE-SEM images of the products with different temperatures were shown in the supplementary material. It was clearly observed that all of the samples were consistent with the Ni_3Se_2 (JCPDS no. 85-0754) in Fig. S1 and the morphology of each group of samples were not significantly changed with different temperatures, as displayed in Fig. S2. To investigate the suitable synthesis temperatures for irregular film, nanowire arrays and microsphere of Ni_3Se_2 on electrochemical performance, the samples with different morphologies synthesized with 140 °C, 160 °C and 180 °C were also prepared. All the samples were analyzed by galvanostatic charge/discharge (GCD) measurement in 3 M KOH at the current density of 10 mA/cm^2, and the results were presented in Fig. 3. Figure 3a shows the GCD curves of Ni_3Se_2-A with different synthesis temperatures, compared to the 140 °C and 180 °C, the sample with 160 °C exhibits longer discharge time, indicating the suitable synthesis temperature for the irregular film of Ni_3Se_2 is 160 °C. And the areal specific capacitance (C_s) and gravimetric specific capacitance (C_m) were calculated according to the formula [28]:

$$C_s = (I \times \Delta t)/(S \times \Delta V) \quad (1)$$

$$C_m = (I \times \Delta t)/(m \times \Delta V), \quad (2)$$

where C_s (F/cm^2) is the areal specific capacitance, and C_m (F/g) is the gravimetric specific capacitance, and the I, Δt, S, m and ΔV are the discharge current (A), discharge time (s), the effective area of electrode (cm^2), the weight of active material (g) and the voltage variation (V), respectively. Thus, it can be calculated that the C_s of the Ni_3Se_2-A at 160 °C (1.26 F/cm^2) is higher than that of 140 °C (1.19 F/cm^2) and 180 °C (0.97 F/cm^2). The GCD curves of Ni_3Se_2-B with different synthesis temperatures are shown in Fig. 3b, it can be clearly observed that the discharge time of the sample with 140 °C is longer than that of 160 °C and 180 °C, and the corresponding areal-specific capacitance is calculated to be 1.48 F/cm^2, 1.23 F/cm^2 and 1.00 F/cm^2, respectively.

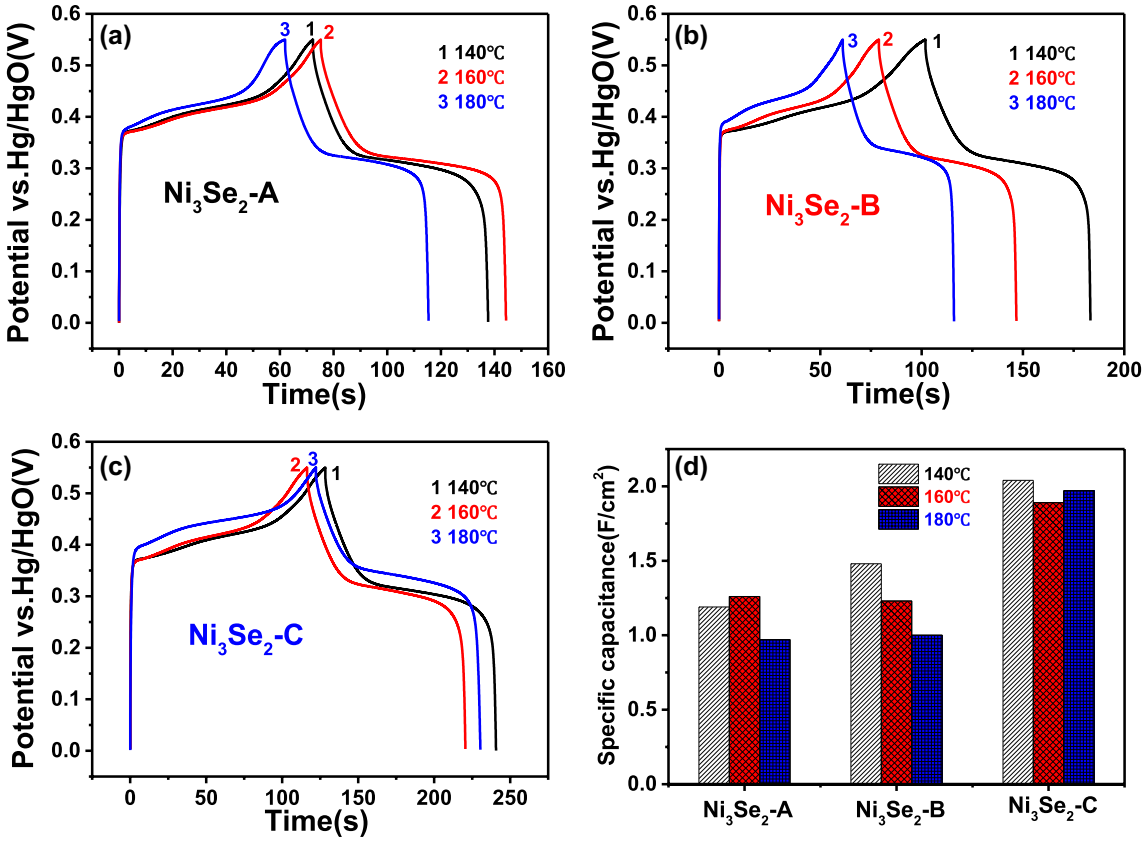

Fig. 3 GCD curves of Ni_3Se_2@Ni synthesized with different temperature: **a** Ni_3Se_2-A, **b** Ni_3Se_2-B, **c** Ni_3Se_2-C; **d** histogram of specific capacitance comparison

Meanwhile, the GCD curves of the Ni_3Se_2-C with different synthesis temperatures are displayed in Fig. 3c. It can be seen that the sample with 140 °C presents the longest discharge time, indicating the C_s of the sample at 140 °C (2.04 F/cm^2) is higher than that of 160 °C (1.89 F/cm^2) and 180 °C (1.97 F/cm^2). From what has been discussed above, we can draw the conclusion that the electrochemical properties of Ni_3Se_2 with different morphologies are different at different synthesis temperatures. It may be caused by the different crystallinity of the materials with different synthesis temperatures, which would lead to the difference of carrier mobility [29]. However, the performances of electrodes with different morphologies with different synthesis temperature are not very different, which may be due to the small change in crystallinity, as shown in Fig. S1. Besides, to compare the electrochemical performance of the samples with different morphologies and temperatures more intuitively, a histogram between C_s and different samples are performed in Fig. 3d. It can be seen that the optimum temperatures for Ni_3Se_2-A (irregular film), Ni_3Se_2-B (nanowire arrays) and Ni_3Se_2-C (microsphere) are 160 °C, 140 °C and 140 °C, respectively.

The electrochemical performance of Ni_3Se_2@Ni with irregular film, nanowire arrays and microsphere morphologies synthesized with corresponding optimum temperature is compared in Fig. 4. Figure 4a displays the cyclic voltammetry (CV) curves of Ni_3Se_2@Ni with different morphologies and bare nickel foam electrode at a scan rate of 30 mV/s. It can be clearly observed that the internal area of the CV curve of nickel foam closes to zero, indicating the capacitance contribution of nickel foam can be neglected. In addition, it can also be seen that the internal area of the CV curve of Ni_3Se_2-C is larger than that of Ni_3Se_2-A and Ni_3Se_2-B, revealing the higher capacitance of Ni_3Se_2-C. Figure 4b shows the GCD curves of Ni_3Se_2@Ni with different morphologies at the current density of 10 mA/cm^2. It is evident that the Ni_3Se_2-C presents longer charge/discharge time than that of the Ni_3Se_2-A and Ni_3Se_2-B, revealing the better electrochemical performance of Ni_3Se_2-C, which is consistent with the CV results. The GCD curves of Ni_3Se_2@Ni with different morphologies under different current densities were performed and the corresponding areal specific capacitances were also calculated, as shown in Fig. 4c. The results show that the specific capacitances of Ni_3Se_2-C are higher than that of Ni_3Se_2-B and Ni_3Se_2-A at the given current densities, revealing that the Ni_3Se_2 with microsphere morphology (Ni_3Se_2-C) displays the best electrochemical

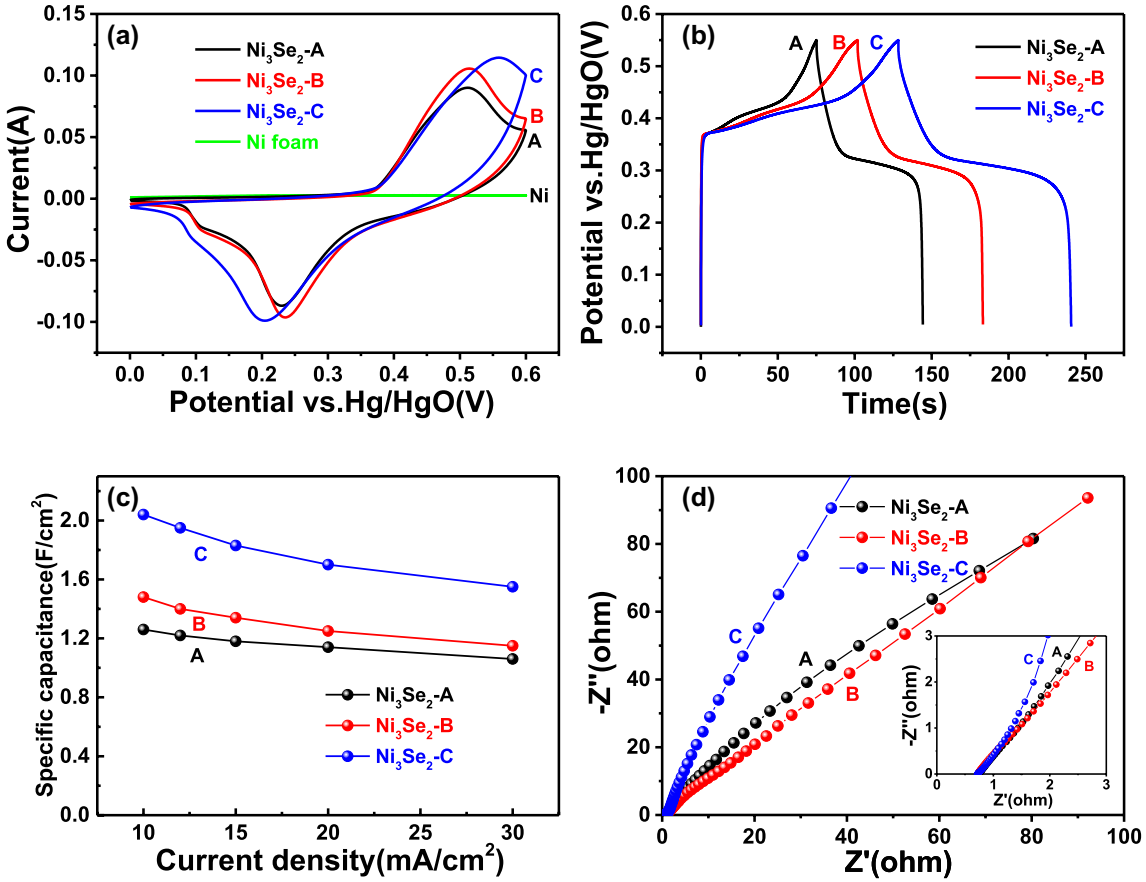

Fig. 4 Electrochemical performance comparison of Ni_3Se_2-A, Ni_3Se_2-B and Ni_3Se_2-C prepared at 160 °C, 140 °C and 140 °C, and bare nickel foam, respectively: **a** CV curves at the scan rate of 30 mV/s; **b** GCD curves at the current density of 10 mA/cm^2; **c** specific capacitance at different current densities; **d** EIS in the frequency region of 0.01 Hz to 100 kHz, inset is an enlarged view of the high frequency region

performance followed by nanowire arrays (Ni_3Se_2-B) and irregular film (Ni_3Se_2-A) morphologies. This difference in electrochemical performance may be due to the fact that different morphologies may provide different active sites [27]. Compared with the film and nanowires morphologies, the microsphere can provide more active sites and larger ion channels which is beneficial to improve the electrochemical performance [30]. Furthermore, the electrochemical impedance spectroscopy (EIS) of Ni_3Se_2 with different morphologies is shown in Fig. 4d with the frequency region of 10^{-2}–10^5 Hz, which reveals that the internal resistance (R_s) of Ni_3Se_2-A, Ni_3Se_2-B and Ni_3Se_2-C is 0.75 Ω, 0.73 Ω and 0.72 Ω, respectively, which can be clearly seen in the inset in Fig. 4d. The plots in the low frequency region correspond to the diffusion control regions, and the slope of these plots is related to the diffusion resistance. There is no significant difference in the R_s, but the Ni_3Se_2-C has a maximum slope, indicating the lowest diffusive resistance of the Ni_3Se_2-C electrode.

Nitrogen adsorption–desorption tests were performed to measure the specific surface area (SSA) and the pore size distribution of Ni_3Se_2-A, Ni_3Se_2-B and Ni_3Se_2-C prepared at 160 °C, 140 °C and 140 °C. As shown in Fig. 5a, all of them exhibited a typical behavior of type IV isotherms according to the IUPAC classification, suggesting that it is consisted predominantly of mesoporous [31]. The BET specific surface area of 4.74 m^2/g, 7.17 m^2/g and 17.35 m^2/g were obtained for Ni_3Se_2-A, Ni_3Se_2-B and Ni_3Se_2-C, respectively. The Ni_3Se_2-C with microsphere morphology displayed the largest BET SSA compared with Ni_3Se_2-A and Ni_3Se_2-B, and the result well agreed with the observation of SEM. The BJH method was used to calculating the pore size distribution of the samples, as shown in Fig. 5b. The average pore size of Ni_3Se_2-A, Ni_3Se_2-B and Ni_3Se_2-C were calculated to be 114.9 nm, 140.4 nm and 79.4 nm, and the pore volume were 0.014 cm^3/g, 0.025 cm^3/g and 0.034 cm^3/g, respectively. The results indicated that the Ni_3Se_2-C have a suitable mesoporous distribution with more electroactive sites and

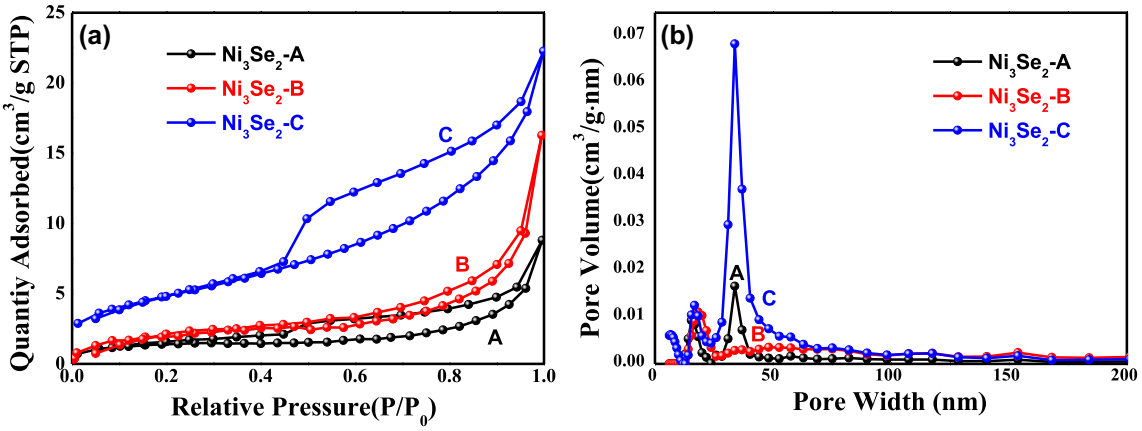

Fig. 5 **a** Nitrogen adsorption and desorption isotherms and **b** pore size distribution of Ni_3Se_2-A, Ni_3Se_2-B and Ni_3Se_2-C prepared at 160 °C, 140 °C and 140 °C

ion-transport pathways, which is beneficial to improve the electrochemical performance [32].

From the above discussion, it is known that the Ni_3Se_2 with microsphere morphology (Ni_3Se_2-C) displays the best electrochemical performance. And thus, the electrochemical performance of Ni_3Se_2-C was further study in detail, as presented in Fig. 6. The CV curves of Ni_3Se_2-C at scan rates from 5 to 50 mV/s are shown in Fig. 6a. It can be observed that the CV curves consist of a

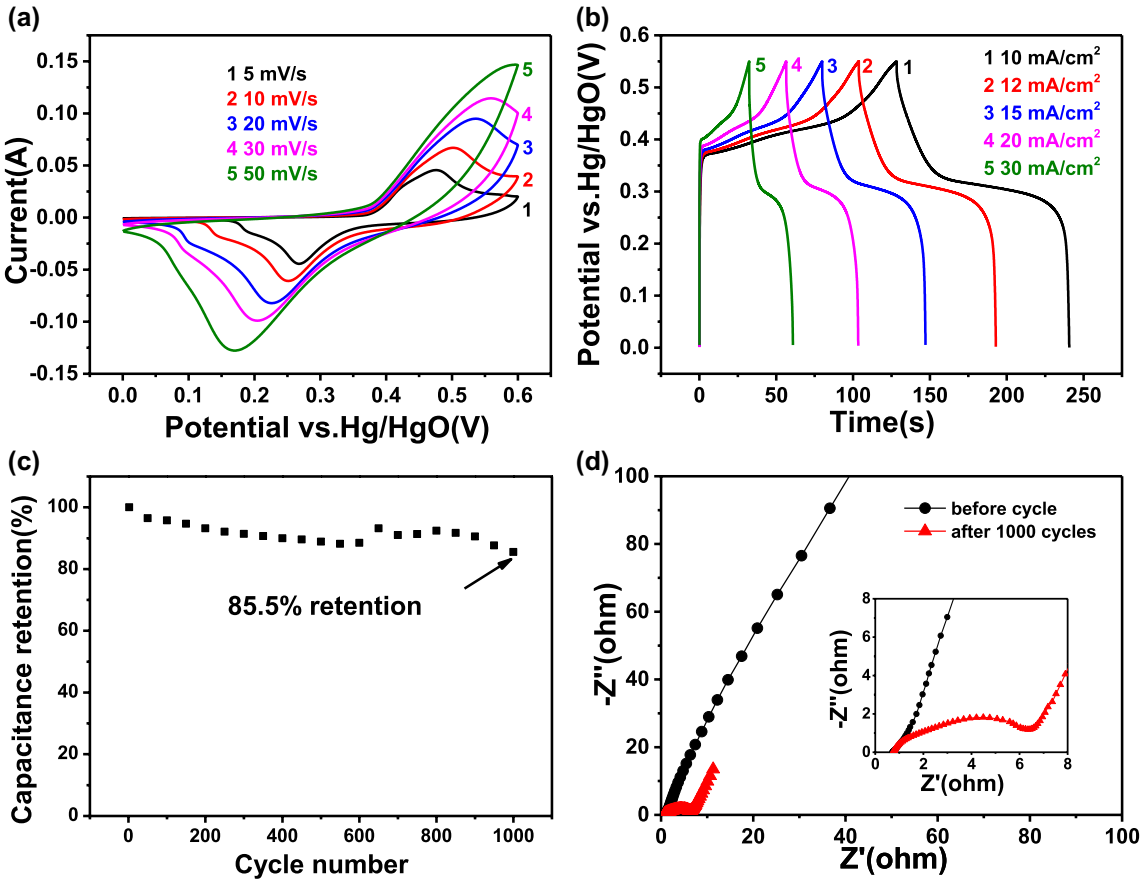

Fig. 6 Electrochemical performance of Ni_3Se_2-C: **a** CV curves at different scan rates; **b** GCD curves at different current densities; **c** cycling stability for charging/discharging 1000 times; **d** EIS plots before and after 1000 cycles, inset is an enlarged view of the high-frequency region

pair of redox peaks, which may be from the contribution of the redox reaction below [33]:

$$Ni_3Se_2 + 3OH^- \leftrightarrow Ni_3Se_2(OH)_3 + 3e^-. \quad (3)$$

Moreover, the current response is increased with the increase of scan rate, but the peak shape is still maintained well, indicating the good rate performance. And then the capacitive performance of Ni_3Se_2-C at different current densities was identified by GCD measurements, as shown in Fig. 6b. According to the GCD curves and Eqs. (1) and (2), the areal specific capacitances of Ni_3Se_2-C electrode under the current densities of 10, 12, 15, 20 and 30 mA/cm^2 is 2.04, 1.95, 1.83, 1.70 and 1.55 F/cm^2, and the corresponding gravimetric specific capacitance is 816, 780, 732, 680 and 620 F/g, respectively. Notably, the gravimetric specific capacitance value of Ni_3Se_2-C at 10 mA/cm^2 (corresponding to 4 A/g) is higher than that of the previous report (693.8 F/g at 4 A/g) [25]. And then the specific capacitance of Ni_3Se_2 in this work and some other Ni_xSe_y electrode materials with different morphologies are compared, as presented in Table 1. We can see that a series of nickel selenide with ratio of Ni/Se of 1.5, 1, 0.85 and 0.5 [34, 35] exhibits good electrochemical performance. However, the ratio of Ni/Se is not the key factor affecting the electrochemical performance which is mainly affected by morphology and structure. Generally, the larger the specific surface area of nanomaterial is, the better the electrochemical performance will be. As shown in Table 1, the specific capacitance of microspheres of Ni_3Se_2, denser nanorod arrays of NiSe, ball-like structure of $Ni_{0.85}Se$ and truncated cube-like structure of $NiSe_2$ is higher than that of other morphologies under the corresponding ratio of Ni/Se. Although the specific capacitance of Ni_3Se_2 in this work is not the best, it is still better than that of NiSe with the same morphology of microspheres [22].

Furthermore, the long-term cycling stability of Ni_3Se_2-C was studied at a current density of 30 mA/cm^2 for 1000 cycles, as shown in Fig. 6c. It can be observed that the Ni_3Se_2-C exhibits good long-term stability with 85.5% of specific capacitance retention after 1000 cycles. Besides, the EIS was used to investigate the resistance variation before and after 1000 cycles. It has been obtained above that the R_s of Ni_3Se_2-C with microsphere morphology before cycle is 0.72 Ω, however, the R_s only increases to 0.77 Ω after 1000 cycles, and the corresponding charge transfer resistance (R_{ct}) increases to 7.93 Ω. The increase of charge transfer resistance may be due to the microstructural change effect after 1000 cycles [36]. Thus, the morphology of Ni_3Se_2-C after 1000 cycles is further investigated in Fig. 7b. To see the changes before and after 1000 cycles clearly, the FE-SEM images of Ni_3Se_2-C before and after cycles are compared in Fig. 7. It can be observed from the low-magnification image in Fig. 7b that the morphology of Ni_3Se_2-C after 1000 cycles is still microsphere, however, the diameter of microsphere increases slightly relative to the initial size in Fig. 7a. By

Table 1 The specific capacitance comparison of Ni_xSe_y with different morphologies

No	Ni/Se	Materials	Morphology	C_s (F/cm^2)	I (mA/cm^2)	C_m (F/g)	I (A/g)	Ref.
1	1.5	Ni_3Se_2	Microspheres	2.04	10	816	4	This work
2	1.5	Ni_3Se_2	Nanowire arrays	1.48	10	592	4	This work
3	1.5	Ni_3Se_2	Irregular film	1.26	10	504	4	This work
4	1.5	Ni_3Se_2	Nanosheets	1.71	2	854	1	[25]
5	1.5	Ni_3Se_2	Nanosheets	1.39	8	693.8	4	[25]
6	1	NiSe	Hierarchical microspheres	0.74	2.3	492	0.5	[22]
7	1	NiSe	Coarse and irregular surface	4.98 (at 2 mV/s)	\	\	\	[24]
8	1	NiSe	Uneven nanorod arrays	5.96 (at 2 mV/s)	\	\	\	[24]
9	1	NiSe	Denser nanorod arrays	7.5 (at 2 mV/s)	\	\	\	[24]
10	1	NiSe	Nanowire film	5.01	\	1790	5	[17]
11	0.85	$Ni_{0.85}Se$	Rough film	1.34	1.2	1115	1	[21]
12	0.85	$Ni_{0.85}Se$	Rough film	0.98	4.8	815.3	4	[21]
13	0.85	$Ni_{0.85}Se$	Nanoparticle	\	\	1101	3	[27]
14	0.85	$Ni_{0.85}Se$	Ball-like structure	\	\	1539	3	[27]
15	0.85	$Ni_{0.85}Se$	Flower-like structure	\	\	1752	3	[27]
16	0.5	$NiSe_2$	Truncated cube-like	4.07	11.7	1044	3	[23]
17	0.5	$NiSe_2$	Truncated cube-like	3.7	19.5	948	5	[23]
18	0.5	$NiSe_2$	Hexapod-like	\	1	75	\	[34]
19	0.5	$NiSe_2$	Hollow spheres	\	\	341	1	[35]
20	0.5	$NiSe_2$	Hollow spheres	\	\	322	5	[35]

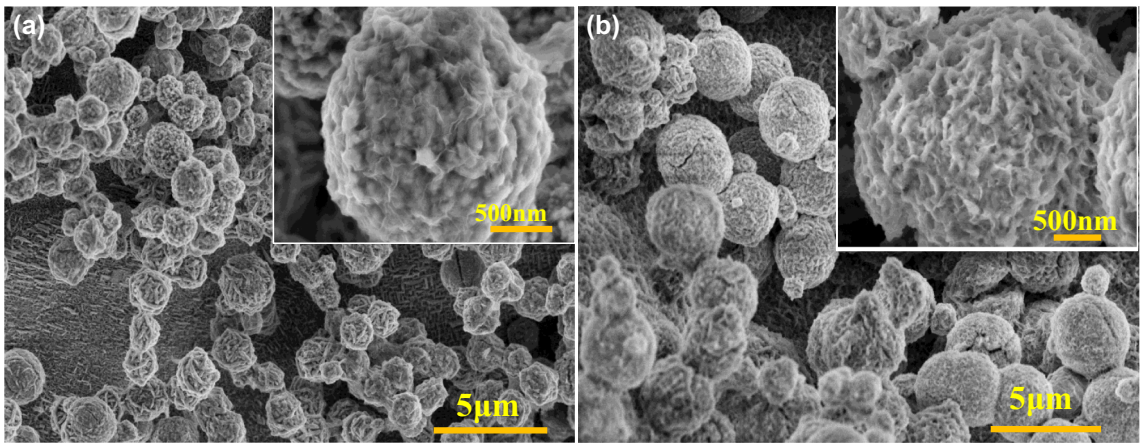

Fig. 7 FE-SEM images of Ni_3Se_2-C: **a** before cycle, **b** after 1000 cycles, the insets are the corresponding images of partial enlargement

further observation of the high-magnification images of inset in Fig. 7, it can be seen that the microsphere surface of Ni_3Se_2-C after 1000 cycles become rougher, which further verifies that there is a slight change in the microstructure.

4 Conclusions

In a word, the Ni_3Se_2 with irregular film, nanowire arrays and microsphere morphologies in situ growth on nickel foam were successfully synthesized by a simple one-step hydrothermal method and the electrochemical performance was discussed. The results show that the Ni_3Se_2 with microsphere morphology (Ni_3Se_2-C) displays better electrochemical performance with areal-specific capacitance of 2.04 F/cm^2 (corresponding gravimetric specific capacitance is 816 F/g) at the current density of 10 mA/cm^2 (4 A/g). Meanwhile, the Ni_3Se_2 with microsphere morphology exhibits good long-term stability with 85.5% of specific capacitance retention after 1000 cycles. The results indicated that the Ni_3Se_2@Ni could be used as a high-performance electrode for energy storage devices.

Acknowledgements This study was supported by the National Natural Science Foundation of China (51564009), Natural Science Foundation of Guangxi Province (2016GXNSFBA380190, 2018GXNSFAA138041, 2015GXNSFDA139035 and 2018JJA160029), Open Project Fund of Guangxi Ministry-Province Jointly-Constructed Cultivation Base for State Key Laboratory of Processing for Non-ferrous Metal and Featured Materials (14KF-10), the Doctoral Scientific Research Project of Guilin University of Technology and Guangxi Key Laboratory in Universities of Clean Metallurgy and Comprehensive Utilization for Non-ferrous Metals Resources.

Compliance with ethical standards

Conflict of interest The authors declare that they have no conflict of interest.

References

1. B.R. Wiston, M. Ashok, Mater. Lett. **235**, 76–79 (2019)
2. S. Thakur, S. Maiti, T. Paul, N. Besra, S. Sarkar, K.K. Chattopadhyay, CrystEngComm **20**, 6183–6196 (2018)
3. A.A. Yadav, Y.M. Hunge, S.B. Kulkarni, J. Mater. Sci. Mater. Electron. **29**, 16401–16409 (2018)
4. Y. Jang, J. Jo, Y.M. Choi, I. Kim, S.H. Lee, D. Kim, S.M. Yoon, Electrochim. Acta **102**, 240–245 (2013)
5. G. Lota, T.A. Centeno, E. Frackowiak, F. Stoeckli, Electrochim. Acta **53**, 2210–2216 (2008)
6. N.G. Sahoo, H.K.F. Cheng, L. Li, S.H. Chan, Z. Judeh, J. Zhao, Adv. Funct. Mater. **19**, 3962–3971 (2009)
7. M.B. Tayel, M.M. Soliman, S. Ebrahim, M.E. Harb, Synth. Met. **217**, 237–243 (2016)
8. K. Wang, X. Dong, C. Zhao, X. Qian, Y. Xu, Electrochim. Acta **152**, 433–442 (2015)
9. F. Wang, X. Lv, L. Zhang, H. Zhang, Y. Zhu, Z. Hu, Y. Zhang, J. Ji, W. Jiang, J. Power Sources **393**, 169–176 (2018)
10. X. Gao, H. Yue, E. Guo, L. Yao, X. Lin, B. Wang, E. Guan, D. Bychanok, J. Mater. Sci. Mater. Electron. **28**, 17939–17947 (2017)
11. V. Gupta, N. Miura, Electrochim. Acta **52**, 1721–1726 (2006)
12. S.R. Sivakkumar, W.J. Kim, J.-A. Choi, D.R. MacFarlane, M. Forsyth, D.-W. Kim, J. Power Sources **171**, 1062–1068 (2007)
13. R. Kotz, M. Carlen, Electrochim. Acta **45**, 2483–2498 (2000)
14. D. He, S. Xing, B. Sun, H. Cai, H. Suo, C. Zhao, Electrochim. Acta **210**, 639–645 (2016)
15. W. Sun, L. Xiao, X. Wu, J. Alloys Compd. **772**, 465–471 (2019)
16. L. Mi, H. Sun, Q. Ding, W. Chen, C. Liu, H. Hou, Z. Zheng, C. Shen, Dalton Trans. **41**, 12595–12600 (2012)
17. C. Tang, Z. Pu, Q. Liu, A.M. Asiri, X. Sun, Y. Luo, Y. He, ChemElectroChem **2**, 1903–1907 (2015)
18. Q. Jiang, R. Chen, H. Chen, J. Jiang, X. Yang, Y. Ju, R. Ji, Y. Zhang, J. Mater. Sci. **53**, 7672–7682 (2018)
19. K.S. Bhat, H.S. Nagaraja, Int. J. Hydrogen Energy **43**, 19851–19863 (2018)
20. X. Li, S. Li, Z. Zhang, C. Liu, B. Qu, J. Pu, Mater. Lett. **220**, 86–89 (2018)
21. C. Gong, M. Huang, J. Zhang, M. Lai, L. Fan, J. Lin, J. Wu, RSC Adv. **5**, 81474–81481 (2015)
22. K. Guo, F. Yang, S. Cui, W. Chen, L. Mi, RSC Adv. **6**, 46523–46530 (2016)
23. S. Wang, W. Li, L. Xin, M. Wu, Y. Long, H. Huang, X. Lou, Chem. Eng. J. **330**, 1334–1341 (2017)

24. Y. Tian, Y. Ruan, J. Zhang, Z. Yang, J. Jiang, C. Wang, Electrochim. Acta **250**, 327–334 (2017)
25. S. Jiang, J. Wu, B. Ye, Y. Fan, J. Ge, Q. Guo, M. Huang, J. Mater. Sci. Mater. Electron. **29**, 4649–4657 (2018)
26. L. Cheng, M. Xu, Q. Zhang, G. Li, J. Chen, Y. Lou, J. Alloys Compd. **781**, 245–254 (2019)
27. S. Ma, S. Zhou, S. Wang, M. Liu, J. Alloys Compd. **728**, 592–599 (2017)
28. Y. Yuan, R. Chen, H. Zhang, Q. Liu, J. Liu, J. Yu, C. Wang, Z. Sun, J. Wang, Electrochim. Acta **294**, 325–336 (2019)
29. I. Shakir, M. Shahid, H.W. Yang, D.J. Kang, Electrochim. Acta **56**, 376–380 (2010)
30. Y. Zhang, J. Zheng, Y. Zhao, T. Hu, Z. Gao, C. Meng, Appl. Surf. Sci. **377**, 385–393 (2016)
31. W. Chen, C. Xia, H.N. Alshareef, ACS Nano **8**, 9531–9541 (2014)
32. G. Zhou, F. Li, H.-M. Cheng, Energy Environ. Sci. **7**, 1307–1338 (2014)
33. H. Huo, Y. Zhao, C. Xu, J. Mater. Chem. A **2**, 15111 (2014)
34. N.S. Arul, J.I. Han, Mater. Lett. **181**, 345–349 (2016)
35. M. Lu, X.-P. Yuan, X.-H. Guan, G.-S. Wang, J. Mater. Chem. A **5**, 3621–3627 (2017)
36. M. Huang, F. Li, Y.X. Zhang, B. Li, X. Gao, Ceram. Int. **40**, 5533–5538 (2014)